PIER M

(Received 28 August 2023, Accepted 20 November 2023, Scheduled 2 December 2023)

Design, Modeling and Analysis of Low Cross Polarization Level Low Radar Cross Section Conformal Ultra Wideband Absorber based on Resistive Metasurface

Saurabh K. Srivastava, Rahul Dubey, and Manoj K. Meshram*

Department of Electronics Engineering, Indian Institute of Technology (BHU), Varanasi, Varanasi 221005, India

ABSTRACT: In this paper, a low cross-polarization level, low radar cross section (RCS), conformal, ultra-wideband, polarization-insensitive absorber utilizing sinusoidal periphery annular ring (SPAR) resonator based novel resistive metasurface is presented. The proposed absorber operates with more than 90% absorptivity over the frequency range 7.68 GHz–24.90 GHz encompassing *X*-, *Ku*- and major portion of *K*-bands. The absorber consists of two sinusoidal peripheries annular rings embedded with lumped resistors, placed on top of a 0.1 mm thin low cost FR-4 substrate which is supported by metal backed foam. The sinusoidal periphery on the annular rings improves the absorption bandwidth and miniaturizes the proposed structure. Cross-polarized reflected component from the absorber is also investigated and included in the estimation of absorptivity to validate that the proposed structure functions as an absorber and not as a reflective type polarization converter. An equivalent circuit analysis based on the transmission line model is also presented. Novelty of the proposed article's lies in the design approach for the proposed absorber in which flexibility is incorporated to choose unit cell geometrical parameters as per the limiting frequencies (upper and lower) of desired band along with some miniaturization aspects of the absorbing structure. Furthermore, 10 dB RCS reduction is discussed, and the formula is derived by including cross-polarized reflection component of the incident wave in estimation. The proposed absorber is validated through theoretical, simulation, and experimental studies for planar and conformal applications.

1. INTRODUCTION

In recent years, the research on metamaterial or metasurface based absorber has gained momentum due to its compact size and light weight, compared to the conventional absorber [1]. These artificially engineered structures have ability to control electromagnetic waves. Landy et al. first experimentally demonstrated a perfect metamaterial absorber having narrow bandwidth [2]. Subsequently, various types of multiband [3–5], wideband absorbers have been reported [6–9]. However, a limitation of many of the reported structures is the lack of information regarding their cross-polarized reflected component (CPRC) of incident waves. Considering the CPRC of the incident wave in absorptivity estimation, absorptivity level drastically decreases from 90% to below 20% over the claimed operating band [10–12]. Therefore, it is necessary to investigate the CPRC of incident wave. Recently, broadband absorption has been achieved with a low cross polarization level through the utilization of an anti-reflecting metasurface [13]. Although these are simple unit cell structures, without introducing large amounts of ohmic or dielectric loss, it is very difficult to achieve ultra-wideband absorption. Moreover, all of these rigid absorbers have a very limited scope, when it comes to non-planar surfaces. In practical scenarios where absorbers need to be deployed over curved surfaces, there is growing demand for conformal ultra-wideband absorbers. Consequently, the substrate must possess flexible or conformal characteristics to meet these requirements.

By using various additive manufacturing methods, conformal absorbers based on frequency selective surfaces (FSSs)/metamaterials (MTMs) have been investigated [14–22]. In [14], a single band flexible metamaterial (MTM) conformal absorber was fabricated using a thin FR-4 substrate. In [15], Hakla et al. designed a dual-band conformal MTM absorber. By using a GML 1000 substrate, a polarization-insensitive conformal MTM absorber for dual and triple band applications was presented in [16]. Recently, in [17], Kumar et al. presented low cross polarization level, convolved frequency selective surface (FSS) based absorbers for *X*-band application. However, due to resonant behavior, these absorbers suffer from narrow bandwidth problems. To overcome this issue, lossy FSSs/MTMs are used. By using inkjet printing technique, an MTM absorber for *X*-band application was presented in which high cost silver nano-particle conductive ink was used on 4 stacked layers of flexible Kodak paper [18]. By using screen printing technique, a conformal absorber for *X*- and *Ku*-bands applications was presented in which graphene nanoflakes with finite resistivity were used on a flexible silicon substrate to achieve wideband absorption [19]. However, printing a resistive pattern on a flexible substrate by using screen printing technique or other additive manufacturing methods has certain drawbacks in obtaining the required optimal surface resistance. The optimal surface

* Corresponding authors: Manoj Kumar Meshram (mkmeshram.ece@iitbhu.ac.in).

resistance depends upon uniform coating, and in the case of FSS it depends upon the FSS shape, permittivity, and thickness of the substrate. In contrast, lumped resistors are available with accurate required resistance value, and by loading it with FSS/MTM, high absorption bandwidth can be achieved. By using lumped resistance, broadband absorption was achieved for part of the C- and complete X-band application [20]. Similarly, in [21], wideband absorption was achieved for complete C- and part of X-band application. In [22], lumped resistors were used as a resistive FSS layer on a polyimide substrate with supporting heavy silicon rubber to achieve broadband absorption for X- and *Ku*-bands. However, as discussed earlier in the case of rigid absorber, these conformal structures [14–16, 19–22] also suffer from lack of information regarding CPRC of incident wave. Moreover, most of the reported conformal absorbers demonstrate their flexibility on curved surfaces, but absorption results on curved surfaces have been rarely discussed in the literature [14, 18].

In this paper, to address above issues, theoretical, simulation, and experimental studies of an ultra-wideband, polarization-insensitive, conformal absorber with low cross polarization level are presented for X-, *Ku*-, and major portion of K-band application. We have demonstrated the design approach for flexibility in choosing unit cell geometrical parameters as per the limiting frequencies (upper and lower) of desired band, while also considering some miniaturization aspects of the structure. To better predict the working principle of the proposed absorber, an equivalent circuit analysis based on the Transmission Line Model (TLM) is also presented. Furthermore, by incorporating the CPRC of incident wave, the radar cross-section (RCS) reduction formula has been derived, and its numerical values are computed for the proposed structure.

2. DESIGN, THEORY AND ANALYSIS

2.1. Design of Unit Cell of Targeted Frequency Range

The schematic of a unit cell of the proposed absorber is shown in Fig. 1(a). The proposed resistive sinusoidal periphery annular ring (SPAR) metasurface-based absorber consists of two quad split resistor loaded rings, which is used as a lossy layer on the top of a 0.1 mm thin low cost FR-4 substrate and supported by metal backed foam. FR-4 substrate having dielectric constant $\varepsilon_r = 4.4$ and loss tangent $\tan\delta = 0.02$ is used for design. The air spacer is used between the substrate and ground plane to broaden the absorption bandwidth. The proposed unit cell is simulated with master/slave boundaries in x- and y-directions with Floquet port in z-direction using ANSYS HFSS v.19.

The design of the proposed ultra wideband absorber is a four-step process. In the first step, targeted frequency bands of interest X-, *Ku*- and major portion of the K-band are chosen. To achieve absorption band over the targeted frequency range, the concept of ring resonator is utilized, whose fundamental frequency is given by $f_o \approx l_{mean}/\sqrt{\varepsilon_{eff}}$, where $l_{mean} = 2\pi R_{mean}$. l_{mean}, R_{mean} are mean length and mean radius of the ring, respectively. ε_{eff} is the effective permittivity of metasurface within stratified media [23]. So we have chosen the two annular rings with different mean radii in such a way that one larger ring operates near the lower frequency of 8.26 GHz, and other smaller ring operates near the higher frequency of 22.9 GHz as shown in Fig. 2(a).

In the second step, by replacing these two annular rings with sinusoidal periphery annular rings, the current flow path of each ring is increased. With the sinusoidal periphery length of the incurved annular ring increased, the resonant frequencies of smaller and larger rings shift towards lower frequency of 21.68 GHz and 7.28 GHz. These rings are represented by Ring 1 and Ring 2, respectively as shown in Fig. 2(a). Ring 1 and Ring 2 consist of the inner and outer radii (r_{1_in} and r_{1_out}) and (r_{2_in} and r_{2_out}) of the sinusoidal periphery, respectively, as shown in Fig. 1(b).

For the i-th ring ($i = 1$ for Ring 1, $i = 2$ for Ring 2), the simplified equation of its inner and outer periphery in parametric form is given by [8]

$$\begin{bmatrix} x(t) \\ y(t) \end{bmatrix} = \begin{bmatrix} r_{i\_in} + k * \sin(n_{i*}t) & 0 \\ 0 & r_{i\_in} + k * \sin(n_{i*}t) \end{bmatrix} \begin{bmatrix} \cos(t) \\ \sin(t) \end{bmatrix} \tag{1}$$

$$\begin{bmatrix} x(t) \\ y(t) \end{bmatrix} = \begin{bmatrix} r_{i\_out} + k * \sin(n_{i*}t) & 0 \\ 0 & r_{i\_out} + k * \sin(n_{i*}t) \end{bmatrix} \begin{bmatrix} \cos(t) \\ \sin(t) \end{bmatrix} \tag{2}$$

where $i = 1, 2$ is used for Ring 1 and Ring 2, respectively. r_{i_in} and r_{i_out} represent the inner and outer radii; n_i represents the angular frequency of i-th ring; k represents the maximum amplitude of inner and outer sinusoidal periphery of each ring. In the third step, predominantly ohmic losses are introduced by creating four splits in each ring and loading it with an adequate value of resistance so that a prominent dip can be observed due to each SPAR, as shown in Fig. 2(b). Finally, in step four, these two resistive rings are combined to form a metasurface unit cell, as depicted in Fig. 1(b). This metasurface unit cell is optimized for the best absorption performance as shown Fig. 2(b) under fabrication tolerance limit of $r_{1\_in} = 2$, $r_{1\_out} = 2.5$, $r_{2\_in} = 4.25$, $r_{2\_out} = 4.75$, $w = L = 0.5$, $h_1 = 0.1$, $h_2 = 4.2$ (unit: mm), $R_{in} = 150\,\Omega$, $R_{out} = 205\,\Omega$, $k = 0.1$, $n_1 = 20$, $n_2 = 40$.

From Fig. 2(b), it is observed that after combining the two resistive rings, there are three distinct resonances in the frequency range of interest, one at 9.62 GHz due to larger ring, another at 24.10 GHz due to smaller ring, and the third at 17.13 GHz due to strong coupling between these resistive rings.

Moreover, this resistor-loaded SPAR metasurface miniaturized the absorbing structure with respect to resistive annular ring without sinusoidal periphery and increased wideband absorption fractional bandwidth from 98% to 105.70% as shown in Fig. 2(c).

2.2. Optimization of the Design

In order to tune the absorption over the targeted frequency range of interest, parametric study of key parameters of absorbing structure is performed.

Firstly, for the widest absorption bandwidth, we examine the adequate value of resistance in each sinusoidal periphery annular ring. Fig. 3(a) shows that at the central resonance frequency

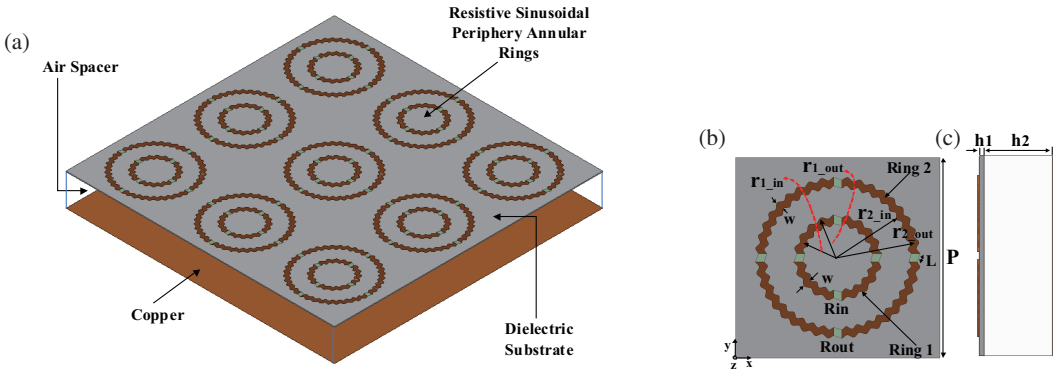

FIGURE 1. Illustration of the geometry of proposed absorber. (a) 3-D view of 3×3-unit cell. (b) Top view of the unit cell. (c) Side view of the unit cell.

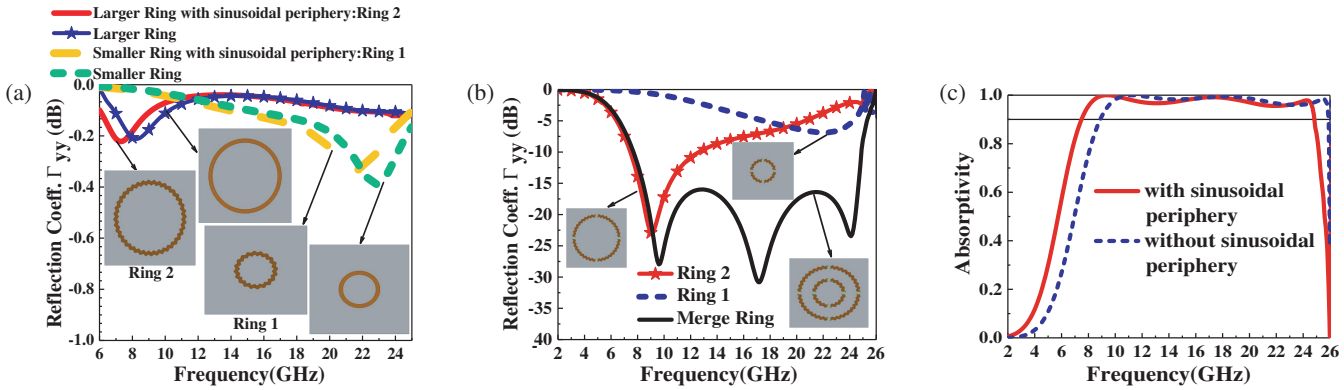

FIGURE 2. Reflection coefficient. (a) For larger ring, smaller ring with and without sinusoidal periphery. (b) For individual and merge Ring 1 and Ring 2 after embedded with chip resistor. (c) Absorptivity response of the proposed structure with and without sinusoidal periphery.

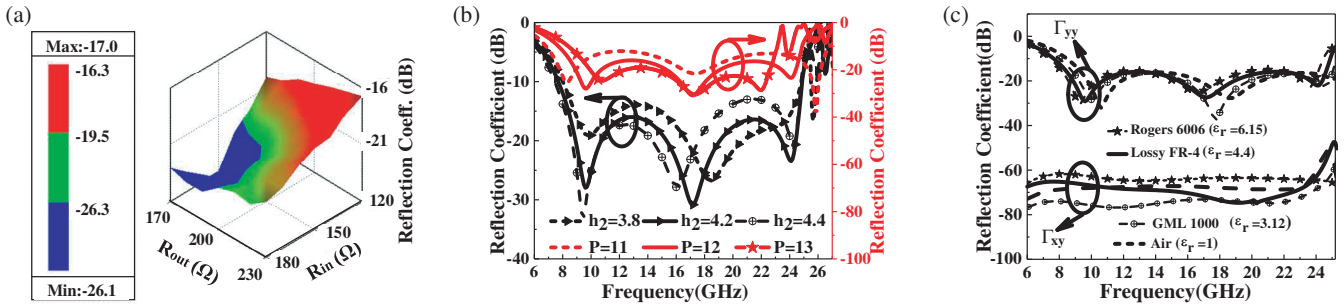

FIGURE 3. Parametric analysis for reflection coefficient. (a) For different values of R_{out} and R_{in} at center frequency of 17.13 GHz. (b) For different values h_2 and P. (c) Co-, cross-polarized reflection coefficient for different substrates.

of 17.13 GHz, the co-polarized reflection coefficient (Γ_{yy}) is less than -15 dB for R_{out} ranging from 170 Ω to 230 Ω and R_{in} ranging from 120 Ω to 180 Ω. Utilizing such degrees of freedom, as per availability, we have chosen $R_{out} = 205\,\Omega$ in the outer ring and $R_{in} = 150\,\Omega$ in the inner rings for fabrication. It gives the best impedance matching of absorbing structure to the free space.

The choice of spacer height h_2 for the widest absorption bandwidth is calculated at central frequency of 17.13 GHz by utilizing the Salisbury screen concept [24, 25],

$$\theta_{el1} + \theta_{el2} = \pi/2 \tag{3}$$

where θ_{el1} and θ_{el2} are the electrical lengths of FR-4 substrate and air spacer, respectively. For predetermined conformal thickness $h_1 = 0.1$ mm of FR-4 substrate, the computed value of θ_{el1} is 4.29° or 0.0238π. Therefore, by using Equation (3), we obtain the value of spacer height as $h_2 \approx 4.2$ mm. Such height provides the best absorption result with a co-polarized reflection coefficient below -15 dB, as depicted in Fig. 3(b). This parametric study of spacer height clearly illustrates that for $h_2 = 3.8$, the bandwidth is small compared to $h_2 = 4.2$, and the higher resonance frequency is less prominent. At -10 dB, the lower cutoff frequency for $h_2 = 4.4$ is slightly lower than $h_2 = 4.2$. However, after the midband frequency, the reflec-

tion curve for $h_2 = 4.4$ is closer to -10 dB than $h_2 = 4.2$. Consequently, we have chosen spacer height $h_2 = 4.2$ as the final optimized parameter, as also supported by the calculation in Equation (3).

Similarly, by keeping the other dimension constant, the influence of periodicity P is also investigated in Fig. 3(b). As periodicity increases, the fringing capacitance between adjacent unit cells decreases [26]. Therefore, weak coupling between adjacent unit cells allows a decrease in absorption bandwidth [27] by shifting the higher frequency towards the lower side and the lower frequency towards the higher side. Therefore, for wideband absorption, an optimized periodicity of $P = 12$ mm is chosen for fabrication.

Therefore, geometrical parameters, such as spacer height, periodicity, and the adequate value of resistances, highly influenced the absorption bandwidth, and they are used as key parameters to tune the absorption bandwidth over the targeted frequency range of interest.

2.3. Performance Discussion and Mechanism of Absorption

Absorptivity performance of the metal backed absorber over the operating band is given by [28]

$$A(\omega) = 1 - |S_{11}(\omega)|^2 \tag{4}$$

where $|S_{11}(\omega)|^2 = |\Gamma_{yy}(\omega)|^2 + |\Gamma_{xy}(\omega)|^2$ represents the reflected power. For y (or TE)-polarized incident wave, the amplitudes of co- and cross-polarized reflection coefficients from the absorber in terms of electric field components can be expressed as $|\Gamma_{yy}| = |\vec{E}_{ry}^{Abs}| \big/ |\vec{E}_{iy}^{Abs}|$ and $|\Gamma_{xy}| = |\vec{E}_{rx}^{Abs}| \big/ |\vec{E}_{iy}^{Abs}|$, respectively. Hence by using (4) and the above expressions, actual absorbed power ($A_{actual}(\omega)$) by the absorber is given by [1]

$$A_{actual}(\omega) = 1 - (|\Gamma_{yy}(\omega)|^2 + |\Gamma_{xy}(\omega)|^2) \tag{5}$$

From (5), it is clear that to maximize actual absorption by the absorber, we have to minimize both cross- and co-polarized reflections generated by incident waves.

Figure 3(c) shows the simulated response of cross- and co-reflection coefficients of the proposed absorber fabricated with a lossy FR-4 substrate. It can be observed that the magnitude of reflection coefficient of CPRC Γ_{xy} is almost negligible, and the co-reflection coefficient is below -10 dB over the frequency range 7.68–24.90 GHz, due to which, 90 % absorptivity is achieved with frequency span of 17.22 GHz over the above operating band.

Further, to demonstrate the proposed absorber's design flexibility, a simulation study is carried out with different substrates, by keeping all the physical dimensions constant, as shown in Fig. 3(c). It can be observed that the magnitude of the CPRC level is negligible and independent of substrate choice.

2.3.1. Effect of Polarization and Incident Angle

From the initial stage of the design our main focus is to maintain the four-fold rotational symmetry in the structure because such a structure generally produces very little cross-polarized reflection. The response of the proposed structure is studied under different polarization angles by changing the polarization angle of the wave from 0° to 90° under normal incidence as shown in Fig. 4(a). It is observed that the absorptivity response remains the same for all polarization angles under normal incidence, which verifies the polarization insensitive characteristic.

Performance of the structure is further investigated under oblique incidence for TE and TM polarizations cases. From Fig. 4(b), it is observed that the structure gives more than 90% absorptivity and quite stable performance up to oblique incidence of 45° under TE polarization case in operating band. However in the case of TM polarization as shown in Fig. 4(c), more than 90% absorptivity is achieved up to oblique incidence of 40°, but higher order harmonics also start generated inside the operating band, and it may be because of grating lobes as the angle of incidence increases from normal to oblique. At oblique incidence free space impedance is different for TM and TE polarizations which is given by [27].

$$Z_o^{TM} = Z_o \cos\theta, \quad Z_o^{TE} = Z_o / \cos\theta \tag{6}$$

For TM polarization free space impedance decreases as angle of incidence increases whereas for TE polarization free space impedance increases. Therefore, due to such an impedance mismatch absorptivity response at oblique incidence is different for TE and TM polarization with respect to normal incidence.

2.3.2. Mechanism of Absorption

To gain insights into the absorption mechanism, the input impedance of the absorber is depicted in Fig. 4(d). It can be observed that its imaginary part is near zero, and the real part is near free space impedance within the absorption band. Therefore, there is minimal reflection from the proposed absorbing structure due to its impedance matching with free space.

Further, Fig. 5 represents the distribution of the real pointing vector over the surface of a unit cell at three resonance frequencies, which provides insight into the behavior of electromagnetic waves within the absorber before they are absorbed. It can be observed that incident power initially propagates along the downward z-direction through the air region and then redirects itself over the metasurface unit cell. This strong convergence of power over the lossy concentric rings and within the substrate leads to strong absorption.

3. EQUIVALENT CIRCUIT ANALYSIS

To better predict the working principle of the proposed conformal absorber equivalent circuit analysis based on Transmission Line Model (TLM) is also presented. The schematic of the top resistive SPAR metasurface and conceptual interpretation of inductive and capacitive effects due to the y-polarized incident wave is shown in Fig. 6(a). Inner and outer resistive ring resonators are modeled as a simplified series combination of the $R_1L_1C_1$ and $R_2L_2C_2$ networks and connected in parallel [29], as shown in Fig. 6(b). However, here resistances R_1 and R_2 are used to represent losses introduced by inner and outer rings, respectively. In this model, C_1 represents the final equivalent capacitance that arises due to the gap between the inner and outer rings. C_2 represents the final equivalent coupling

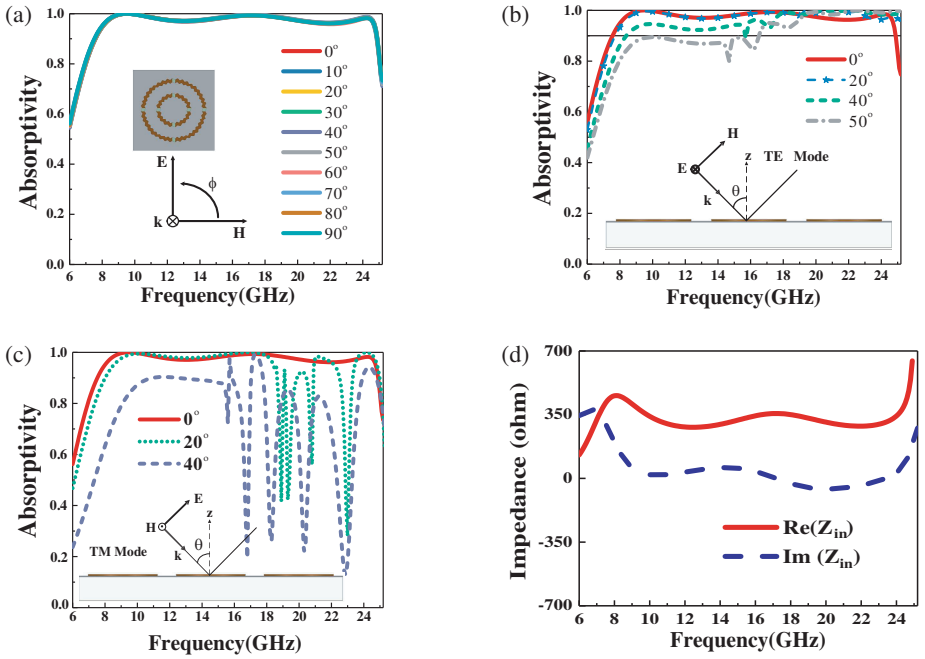

FIGURE 4. (a) Electromagnetic absorption performance for different polarization angle. (b) Electromagnetic absorption performance for oblique incidence under TE polarization. (c) Electromagnetic absorption performance for oblique incidence under TM polarization. (d) Impedance characteristic.

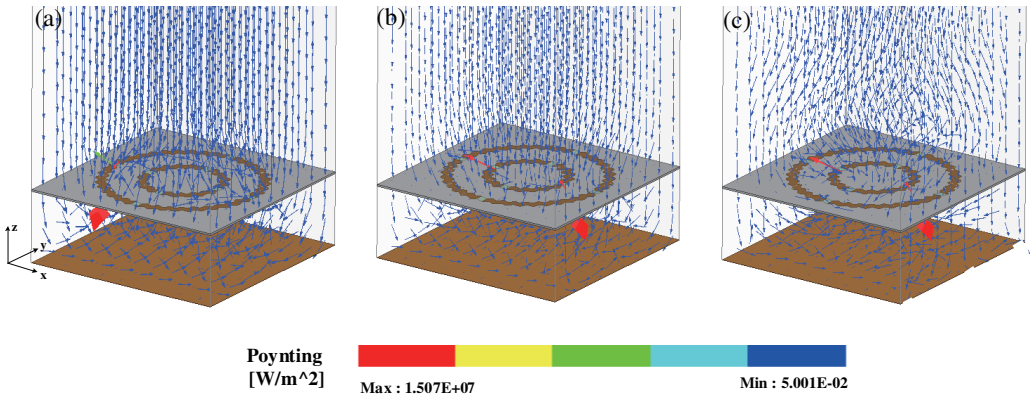

FIGURE 5. Distribution of pointing vector at resonance frequency of (a) 9.6 GHz, (b) 17.1 GHz, (c) 24.1 GHz.

capacitance between the adjacent unit cells. L_1 and L_2 represent the final equivalent inductances of inner and outer rings. The dielectric substrate and air spacer thickness are modeled with transmission line (TL) section (Z_{01}, θ_{el1}) and (Z_{02}, θ_{el2}), where the characteristic impedance of these sections is represented by $Z_{01} = Z_o/\sqrt{\varepsilon_r}$ and $Z_{02} = Z_o$. The ground plane is represented by a short circuit. Therefore, the final simplified qualitative equivalent circuit of the proposed absorber is modeled as shown in Fig. 6(b).

The initial value of inductance L_1, L_2 of the ring is approximated by using a well-defined equation for circular loop [30].

$$L_i(\text{nH}) = 1.257 \times 10^{-3} \times r_{imean} \cdot \left[\ln\left(\frac{r_{imean}}{w_i + t_{cu}}\right) + 0.078\right] \cdot K_g \quad i = 1, 2 \quad (7)$$

where $r_{i\text{-}mean}$, w_i, t_{cu} are dimension in micrometer, and they are mean radius, width, and the copper thickness of the i-th SPAR ring, respectively. K_g is the correction factor that accounts for the presence of the ground plane. Since the ring has an increased periphery with respect to a simple annular ring, this inductance formula is used as an initial approximation for the inductance value of each ring of proposed structure.

From Fig. 6(b), by utilizing the resonance frequency of each *RLC* arm, the initial value of capacitance C_1 due to higher resonance frequency (ω_3) and capacitance C_2 due to lower resonance frequency (ω_1) is determined by using relations (8)

$$C_1 = \frac{1}{\omega_3^2 L_1}, \quad C_2 = \frac{1}{\omega_1^2 L_2} \quad (8)$$

Once the initial value of electrical parameters is obtained using above relation, it is later implemented in Advance De-

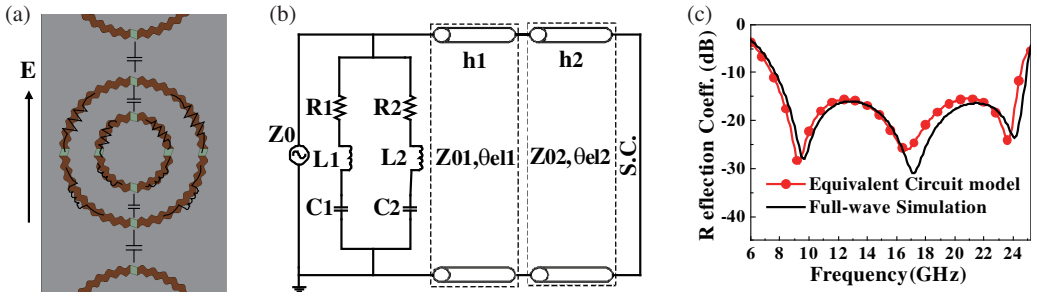

FIGURE 6. (a) Conceptual interpretation of Inductive and Capacitive effect on top resistive SPAR metasurface. (b) Simplified equivalent circuit model of proposed absorber. (c) Comparison of equivalent circuit model with HFSS simulated response.

sign System (ADS) software, where curve fitting technique is used to tune the reflection from circuit model to full-wave EM simulation, and obtain the final lumped parameter as $R_1 = 299.25\,\Omega$, $L_1 = 5.13\,\text{nH}$, $C_1 = 14.34\,\text{fF}$, $R_2 = 337.45\,\Omega$, $L_2 = 13.73\,\text{nH}$, $C_2 = 16.57\,\text{fF}$. The comparison between circuit simulation response and full-wave simulation response is shown in Fig. 6(c). A fair degree of symmetry between these two responses validates the proposed model.

4. ACTUAL RCS ANALYSIS FROM ABSORPTIVITY

With the aim of evaluating the RCS performance from the absorptivity of the proposed resistive metasurface-based absorber, we have applied the fundamental RCS definition. At a far-field distance r away from the target, if $\overrightarrow{E}_s$ is scattered field for $\overrightarrow{E}_\iota$ value of incident field, then RCS is given by [31]

$$\sigma = 10\log_{10}\left(\lim_{r\to\infty} 4\pi r^2 \frac{|\overrightarrow{E}_s|^2}{|\overrightarrow{E}_i|^2}\right)$$

For y-polarized normally incident wave, under Monostatic RCS case $\overrightarrow{E}_s = \overrightarrow{E}_r^{Abs}$, therefore RCS of proposed absorber is given by,

$$\sigma = 10\log_{10}\left(\lim_{r\to\infty} 4\pi r^2 \frac{|\overrightarrow{E}_r^{Abs}|^2}{|\overrightarrow{E}_{iy}^{Abs}|^2}\right) \tag{9}$$

Since the reflected wave not only consists of the co-polarized reflected component but also consists of the cross-polarized reflected component (CPRC), the total reflected electric field at far-field observation point is the vector sum of

$$\begin{aligned}
\overrightarrow{E}_r^{Abs} &= \overrightarrow{E}_{rx}^{Abs} + \overrightarrow{E}_{ry}^{Abs} \\
or\ |\overrightarrow{E}_r^{Abs}|^2 &= |\overrightarrow{E}_{rx}^{Abs} + \overrightarrow{E}_{ry}^{Abs}|^2 = (\overrightarrow{E}_{rx}^{Abs} + \overrightarrow{E}_{ry}^{Abs}) \\
&\quad \cdot(\overrightarrow{E}_{rx}^{Abs} + \overrightarrow{E}_{ry}^{Abs}) \\
&= |\overrightarrow{E}_{rx}^{Abs}|^2 + |\overrightarrow{E}_{ry}^{Abs}|^2 + 2\overrightarrow{E}_{rx}^{Abs} \cdot \overrightarrow{E}_{ry}^{Abs} \\
&= |\overrightarrow{E}_{rx}^{Abs}|^2 + |\overrightarrow{E}_{ry}^{Abs}|^2 + 2|\overrightarrow{E}_{rx}^{Abs}||\overrightarrow{E}_{ry}^{Abs}|\cos\pi/2 \\
&= |\overrightarrow{E}_{rx}^{Abs}|^2 + |\overrightarrow{E}_{ry}^{Abs}|^2 = |\overrightarrow{E}_{iy}^{Abs}|^2(|\Gamma_{xy}|^2 + |\Gamma_{yy}|^2)
\end{aligned} \tag{10}$$

Therefore, by using (9) and (10), the expression for actual RCS reduction $\Delta\sigma_{actual}$ of the proposed absorbing structure with respect to the perfect electric conductor can be calculated by

$$\begin{aligned}
\Delta\sigma_{actual} &= -10\log_{10}\left[\lim_{r\to\infty} 4\pi r^2 \frac{(|\overrightarrow{E}_{iy}^{Abs}|^2(|\Gamma_{yy}|^2 + |\Gamma_{xy}|^2))}{|\overrightarrow{E}_{iy}^{Abs}|^2} \Big/ \right. \\
&\quad \left. \lim_{r\to\infty} 4\pi r^2[1]^2\right] \\
&= -10\log_{10}[|\Gamma_{yy}(\omega)|^2 + |\Gamma_{xy}(\omega)|^2] \qquad (11) \\
&= -10\log_{10}[|S_{11}(\omega)|^2] \\
&= -10\log_{10}[1 - |A_{actual}(\omega)|] \qquad (12)
\end{aligned}$$

Due to the inclusion of CPRC into expression (11), Equation (12) is a well-derived and more generalized formula for RCS reduction than the formula reported in [1, 32]. From (12), we conclude that there is an increase in RCS reduction as the value of $A_{actual}(\omega)$ increases.

To numerically calculate the RCS reduction, both simulated Γ_{yy} and Γ_{xy} or actual absorptivity results of the proposed absorber from Fig. 9(a) are used in expression (11) or (12) and plotted in Fig. 7. It can be observed that the actual RCS reduction of the proposed absorbing structure with respect to the perfect electric conductor exceeds by 10 dB over the frequency range of 7.68–24.90 GHz.

5. FABRICATION AND EXPERIMENTAL VALIDATION

For validation, the prototype of the proposed conformal absorber is fabricated with 15×15-unit cells (180 mm $\times$ 180 mm) on a 0.1 mm thin low cost FR-4 substrate by conventional chemical etching process as shown in Fig. 8(a). Surface mount technology is used to solder the chip resistors of 150 Ω and 205 Ω with 1% tolerance (ERJ2RKF1500X, ERJ2RKF2050X from Panasonic). The fabricated flexible top resistive metasurface used in our design is shown in Fig. 8(b). The measured thickness of the top resistive metasurface is 0.1 mm, as shown in Fig. 8(c). Finally, this metasurface is combined with flexible, lightweight PMI foam [33] ($\varepsilon_r = 1.08$ and $\tan\delta = 0.0052$),

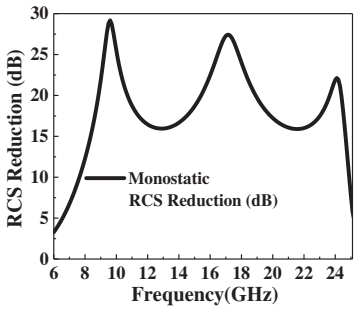

FIGURE 7. Actual monostatic RCS reduction by incorporating cross polarized reflected component of incident wave.

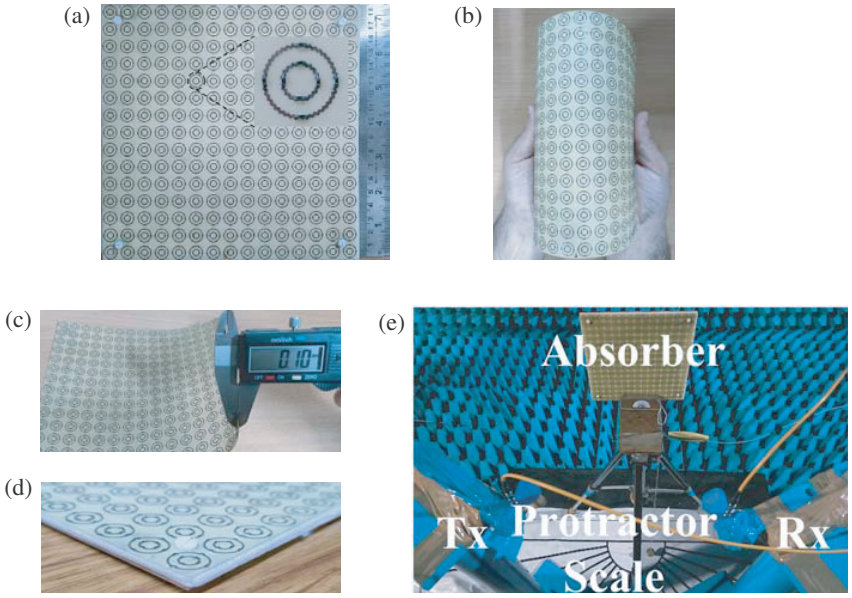

FIGURE 8. (a) Image of fabricated absorber. (b) Flexible top resistive metasurface used in our design. (c) Measured thickness of fabricated conformal top resistive metasurface. (d) Resistive metasurface combined with flexible foam. (e) Measurement setup for Planar absorber.

as depicted in Fig. 8(d). Light weight PMI foam is used in place of air-spacer between the substrate and ground plane to provide mechanical stability for fabricated absorber. Four nylon nuts and bolts are used at four corners of the structure to maintain the 4.2 mm gap between the dielectric and the metal ground plane. The reflection properties of the fabricated sample are measured by free-space measurement technique inside the anechoic chamber. The measurement setup for planar absorber is shown in Fig. 8(e).

During measurement two broadband horn antennas (4–40 GHz) are used, one as a transmitter and the other as a receiver, and connected to Field Fox N9951A handheld analyzer, and the fabricated sample is placed in the far-field region of these antennas. To avoid the mutual coupling between these two horn antennas at lower frequency, they are separated by minimal possible distance. Further copper sheet with the same size as absorbing structure is used to calibrate the absorbing structure to measure actual reflection.

For co-polarized reflection coefficient measurement, the two antennas are placed in the same plane alignment. However, for cross-polarization reflection coefficient measurement, the receiving horn antenna is rotated by 90° with respect to the transmitting horn antenna.

Under the normal incidence, measured and simulated results are plotted in Fig. 9(a). Good agreement is observed between them. However, because of fabrication tolerance, the finite size of periodic sample, the high-frequency parasitic effect of the SMD chip resistor, and inaccuracy in target alignment, there are insignificant discrepancies observed between them. Ripples are observed in measured frequency domain response due to unwanted reflection from environment. One can get rid of these ripples by employing proper time-domain gating function as per availability in the analyzer and improve the measurement accuracy. The measured absorptivity for different polarization angles is shown in Fig. 9(b).

For the TE polarization case, measured absorptivity up to specular angle 40° is shown in Fig. 9(c), and it represents a quite stable performance within the operating band. Similarly, for TM polarization case, the measured absorptivity up to specular angle of 20° is shown in Fig. 9(d).

In order to ensure the adaptability of the proposed absorber for conformal application, absorptivity measurements are carried out with two cylinders with radii of 15.8 cm and 5.5 cm,

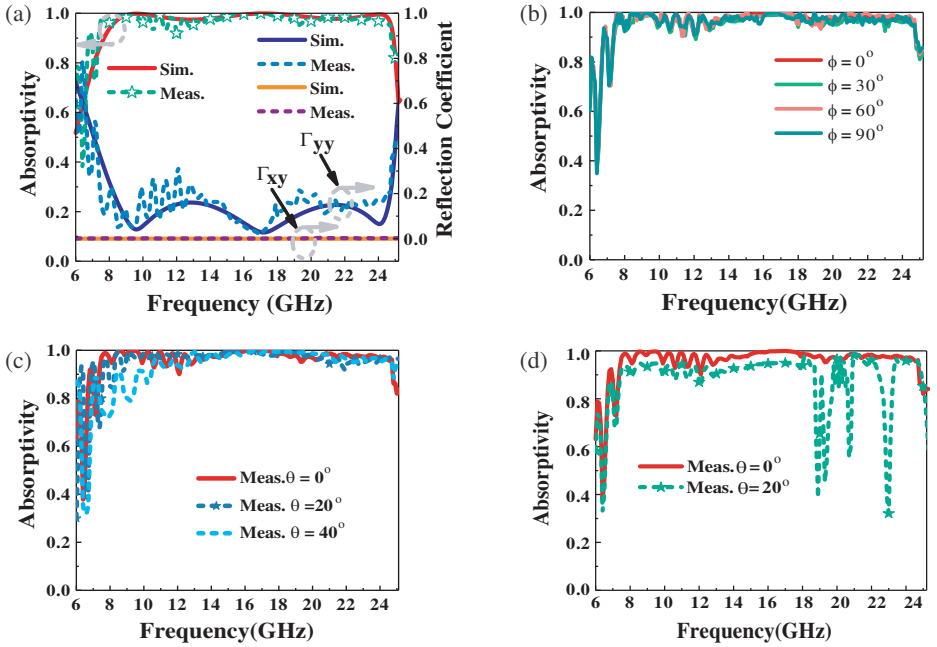

FIGURE 9. Measured results of proposed absorber. (a) For Normal Incidence. (b) For different polarization angle. (c) For oblique incidence under TE Polarization. (d) For oblique incidence under TM Polarization.

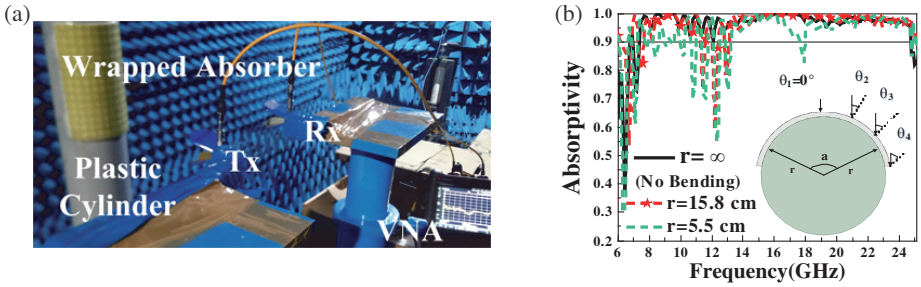

FIGURE 10. (a) Measurement setup for conformal absorber. (b) Measured absorptivity at different bending radii.

which is wrapped by the absorber, as shown in Fig. 10(a). Measurements are performed in a similar manner to the planar absorber. However, the calibration of the absorbing structure is carried out by wrapping a thin copper sheet of the same size around a cylindrical surface. Bending should be done under tolerable limit of SMD resistor. Fig. 10(b) represents the measured results for conformal case 1 (cylinder radius of 15.8 cm), conformal case 2 (cylinder radius of 5.5 cm), and planar case (cylinder radius infinity, no bending). It can be seen that when the planar absorber is wrapped on the cylindrical surface, the absorption performance is slightly deviated at certain points with the decrease of conformal radius. It happens because with plane wave incident normally on the surface of conformal absorber, different areas of the absorber experience different oblique incidences with $\theta_4 > \theta_3 > \theta_2 > \theta_1 = 0°$ as we move along the circumference of bent structure, as shown inside Fig. 10(b). However, the proposed absorber still gives 80% absorption bandwidth in most part of the frequency regime from 7.68 GHz to 24.90 GHz and greater than 90% absorption bandwidth over discrete band.

The performance of the proposed novel resistive SPAR metasurface-based absorber is compared exclusively with other non-transparent conformal reported absorbers in Table 1. Among the conformal configurations where cross-polarized reflection is reported, the proposed structure has much wider fractional bandwidth (FBW), though its periodicity is slightly higher than [18], and thickness is greater than [17] and [18].

In addition, actual RCS reduction is computed in the case of proposed structure whereas it is not estimated in [17–22]. Also, bending angular stability is not experimentally determined in [18]. The inclusion of a low value of cross-polarization level in the estimation of absorptivity and RCS reduction confirms its suitability to work as an absorber rather than a cross-reflective polarization converter. Moreover, last but not least, the most prominent feature of proposed conformal absorber is that it offers design flexibility to choose unit cell geometrical parameters based on the limiting (upper and lower) frequencies of the desired band, along with incorporating some miniaturization aspect of the absorbing structure.

TABLE 1. Comparison of proposed absorber exclusively with non-transparent conformal reported absorber.

Ref.	Year	P mm (λ_L)	t mm (λ_L)	Spectrum (GHz)	FBW (%)	F_D	CPRC	$\Delta\sigma_{\text{actual}}$	Band	Bending Angular Stability or Effect of Bend reported
[17]	2021	10 (0.36)	0.25 (0.009)	10.80–11.09	2.62	Difficult	Yes	No	NB	Yes
[18]	2021	10 (0.28)	1.06 (0.02)	8.43–10.38	20.7	Difficult	Yes	No	BB	No
[19]	2016	15 (0.4)	2 (0.05)	8–19	81.5	Difficult	No	No	WB	Yes
[20]	2017	14.4 (0.29)	3.68 (0.07)	6.08–13.04	72.8	Difficult	No	No	BB	Yes
[21]	2019	12.5 (0.16)	7.57 (0.09)	3.90–10.5	91.6	Difficult	No	No	WB	Yes
[22]	2018	10 (0.25)	3.25 (0.08)	7.6-18.3	82.6	Difficult	No	No	BB	Yes
Pro.	**2023**	**12 (0.30)**	**4.3 (0.11)**	**7.68–24.9**	**105.7**	**Easy**	**Yes**	**Yes**	**UWB**	**Yes**

λ_L: free space wavelength at the lowest operating frequency having absorptivity $> 90\%$, P: Periodicity, t: Thickness, FBW: Fractional Bandwidth, F_D: Design Flexibility to choose unit cell geometrical parameter as per limiting Frequency (lower and upper) of desire band along with some miniaturization aspect of the absorbing structure, CPRC: Cross-polarized reflected component, $\Delta\sigma_{actual}$: 10 dB Actual RCS reduction bandwidth numcerially reported, NB = Narrow band, BB = Broadband, WB = Wideband, UWB = Ultra-wideband.

6. CONCLUSION

In this paper, a conformal, ultra-wideband, polarization-insensitive absorber with a low cross-polarization level and low RCS has been designed and experimentally verified to achieve more than 90% absorptivity over the frequency range of 7.68–24.90 GHz, covering X-, Ku- and major portion of the K-bands. This step-by-step strategically designed approach for a conformal absorber involves the use of a predetermined thickness of a thin FR-4 substrate, exploiting it with an adequate value of resistances, and carefully selecting a well-calculated air spacer height. This approach enables the achievement ultra-wideband absorption while maintaining conformal characteristic. Ultra-wideband width and large RCS reduction are achieved in computation due to the existence of low cross-polarized level for the proposed structure. Conformal behavior, bending angular stability, and polarization insensitivity are several important characteristics that make the proposed absorber a potential candidate in EMI, EMC, RCS reduction, and other military and civil applications.

REFERENCES

[1] Srivastava, S. K., B. Satyanarayana, A. K. Saurabh, and M. K. Meshram, "Low RCS polarization-insensitive ultra wideband absorber based on resistive metasurface," in *2019 IEEE MTT-S International Microwave and RF Conference (IMARC)*, 1–4, Mumbai, India, Dec. 2019.

[2] Landy, N. I., S. Sajuyigbe, J. J. Mock, D. R. Smith, and W. J. Padilla, "Perfect metamaterial absorber," *Physical Review Letters*, Vol. 100, No. 20, 207402, May 2008.

[3] Cao, H., M. Shan, T. Chen, J. Lei, L. Yang, and X. Tan, "Triple-band polarization-independent ultrathin metamaterial absorber," *Progress In Electromagnetics Research M*, Vol. 77, 93–102, 2019.

[4] Ranjan, P., A. Choubey, S. K. Mahto, and R. Sinha, "An ultrathin five-bandpolarization insensitive metamaterial absorber having hexagonal array of 2D-bravais-lattice," in *Progress In Electromagnetics Research C*, Vol. 87, 13–23, 2018.

[5] Xu, G., J. Huang, Z. Ju, Z. Wei, J. Li, and Q. Zhao, "A novel six-band polarization-insensitive metamaterial absorber with four multiple-mode resonators," *Progress In Electromagnetics Research C*, Vol. 77, 133–144, 2017.

[6] Ghosh, S., S. Bhattacharyya, D. Chaurasiya, and K. V. Srivastava, "An ultrawideband ultrathin metamaterial absorber based on circular split rings," *IEEE Antennas and Wireless Propagation Letters*, Vol. 14, 1172–1175, 2015.

[7] De Araujo, J. B. O., G. L. Siqueira, E. Kemptner, M. Weber, C. Junqueira, and M. M. Mosso, "An ultrathin and ultrawideband metamaterial absorber and an equivalent-circuit parameter retrieval method," *IEEE Transactions on Antennas and Propagation*, Vol. 68, No. 5, 3739–3746, May 2020.

[8] Li, S.-J., X.-Y. Cao, J. Gao, T. Liu, Y.-J. Zheng, and Z. Zhang, "Analysis and design of three-layer perfect metamaterial-inspired absorber based on double split-serration-rings structure," *IEEE Transactions on Antennas and Propagation*, Vol. 63, No. 11, 5155–5160, Nov. 2015.

[9] Huang, L., D. R. Chowdhury, S. Ramani, M. T. Reiten, S.-N. Luo, A. J. Taylor, and H.-T. Chen, "Experimental demonstration of terahertz metamaterial absorbers with a broad and flat high absorption band," *Optics Letters*, Vol. 37, No. 2, 154–156, Jan. 2012.

[10] Ahmed, F., T. Hassan, and N. Shoaib, "Comments on "an ultrawideband ultrathin metamaterial absorber based on circular split rings"," *IEEE Antennas and Wireless Propagation Letters*, Vol. 19, No. 3, 512–514, Mar. 2020.

[11] Rahman, S. U., W. Yi, and Q. Cao, "Comments on "an ultrathin and ultrawideband metamaterial absorber and an equivalent-circuit parameter retrieval method"," *IEEE Transactions on Antennas and Propagation*, Vol. 68, No. 12, 8272–8273, Dec. 2020.

[12] Zhang, H., Y. Ma, H. F. Zhang, J. Yang, and J.-X. Liu, "Comment on "frequency tunable low-cost microwave absorber for EMI/EMC application"," *Progress In Electromagnetics Research Letters*, Vol. 78, 39–43, 2018.

[13] Amin, M., A. Fida, A. Rashid, O. Siddiqui, and F. A. Tahir, "Anti-reflecting metasurface for broadband polarization independent absorption at ku band frequencies," *Scientific Reports*, Vol. 12, 2045–2322, Jun. 2022.

[14] Chejarla, S., S. R. Thummaluru, and R. K. Chaudhary, "Flexible metamaterial absorber with wide incident angle insensitivity for conformal applications," *Electronics Letters*, Vol. 55, No. 3, 133–134, Feb. 2019.

[15] Hakla, N., S. Ghosh, K. V. Srivastava, and A. Shukla, "A dual-band conformal metamaterial absorber for curved surface," in *2016 Ursi International Symposium on Electromagnetic Theory (EMTS)*, 771–774, Espoo, Finland, Aug. 2016.

[16] Singh, A. K., M. P. Abegaonkar, and S. K. Koul, "Dual- and triple-band polarization insensitive ultrathin conformal metamaterial absorbers with wide angular stability," *IEEE Transactions on Electromagnetic Compatibility*, Vol. 61, No. 3, 878–886, Jun. 2019.

[17] Kumar, A., G. S. Reddy, and S. Narayan, "Flexible EM wave absorber with high angular stability and low cross polarization reflection level," in *2021 34th General Assembly and Scientific Symposium of the International Union Radio Science (URSI GASS)*, 1–4, Italy, 2021.

[18] Tirkey, M. M. and N. Gupta, "Broadband polarization-insensitive inkjet-printed conformal metamaterial absorber," *IEEE Transactions on Electromagnetic Compatibility*, Vol. 63, No. 6, 1829–1836, Dec. 2021.

[19] Huang, X., K. Pan, and Z. Hu, "Experimental demonstration of printed graphene nano-flakes enabled flexible and conformable wideband radar absorbers," *Scientific Reports*, Vol. 6, Dec. 2016.

[20] Kong, X., X. U. Junyi, M. O. Jin-Jun, and S. Liu, "Broadband and conformal metamaterial absorber," *Frontiers Optoelectron*, Vol. 10, No. 2, 124–131, 2017.

[21] Kalraiya, S., R. K. Chaudhary, and M. A. Abdalla, "Design and analysis of polarization independent conformal wideband metamaterial absorber using resistor loaded sector shaped resonators," *Journal of Applied Physics*, Vol. 125, No. 13, 134904, Apr. 2019.

[22] Chen, H., X. Yang, S. Wu, D. Zhang, H. Xiao, K. Huang, Z. Zhu, and J. Yuan, "Flexible and conformable broadband metamaterial absorber with wide-angle and polarization stability for radar application," *Materials Research Express*, Vol. 5, No. 1, 015804, Jan. 2018.

[23] Costa, F., "A simple effective permittivity model for metasurfaces within multilayer stratified media," *IEEE Transactions on Antennas and Propagation*, Vol. 69, No. 8, 5148–5153, Aug. 2021.

[24] Munk, B. A., *Frequency Selective Surface: Theory and Design*, Wiley, New York, 2000.

[25] Yu, W., G. Q. Luo, Y. Yu, W. Cao, Y. Pan, and Z. Shen, "Dual-polarized band-absorptive frequency selective rasorber using meander-line and lumped resistors," *IEEE Transactions on Antennas and Propagation*, Vol. 67, No. 2, 1318–1322, Feb. 2019.

[26] Carver, K. and J. Mink, "Microstrip antenna technology," *IEEE Transactions on Antennas and Propagation*, Vol. 29, No. 1, 2–24, 1981.

[27] Costa, F., S. Genovesi, A. Monorchio, and G. Manara, "A circuit-based model for the interpretation of perfect metamaterial absorbers," *IEEE Transactions on Antennas and Propagation*, Vol. 61, No. 3, 1201–1209, Mar. 2013.

[28] Wakatsuchi, H., J. Paul, and C. Christopoulos, "Performance of customizable cut-wire-based metamaterial absorbers: Absorbing mechanism and experimental demonstration," *IEEE Transactions on Antennas and Propagation*, Vol. 60, No. 12, 5743–5752, Dec. 2012.

[29] Wang, Z., K. Hashimoto, N. Shinohara, and H. Matsumoto, "Frequency-selective surface for microwave power transmission," *IEEE Transactions on Microwave Theory and Techniques*, Vol. 47, No. 10, 2039–2042, Oct. 1999.

[30] Bahal, I. and P. Bhartia, *Microwave Solid State Circuit Design*, John-Wiley & Sons, Hoboken, NJ, USA, 57–60, 2003.

[31] Balanis, C. A., *Advanced Engineering Electromagnetics*, John-Wiley & Sons, USA, 584, 2012.

[32] Yang, H., X. Y. Cao, J. Gao, W. Li, Z. Yuan, and K. Shang, "Low RCS metamaterial absorber and extending bandwidth based on electromagnetic resonances," *Progress In Electromagnetics Research M*, Vol. 33, 31–44, 2013.

[33] Product information. [Online]. Available: http://www.qdruigao.com/en/